



Variations in Antarctic Peninsula snow liquid water during 1999–2017 revealed by merging radiometer, scatterometer and model estimations

Lei Zheng, Chunxia Zhou*, Qi Liang

Chinese Antarctic Center of Surveying and Mapping, Wuhan University, Wuhan 430079, China

ARTICLE INFO

Edited by Menghua Wang

Keywords:

Snow liquid water
Antarctic Peninsula
SSM/I
QSCAT
ASCAT
RACMO2

ABSTRACT

The Antarctic Peninsula (AP) has recorded one of the strongest warming rates on the Earth since the 1950s, which, however, turned into a cooling trend since 1999. Snow liquid water emerges in the snowpacks in the AP during melt seasons. Monitoring snow liquid water on the AP is critical for evaluating its impacts on the stability, surface mass and energy balances of ice shelves. Most of our knowledge about the occurrence of snow liquid water (OLW) stems from satellite observations and model simulations. However, the relative performances of OLW products derived from these measurements have never been evaluated due to the lack of in-situ snow wetness measurements. We ranked the OLW determined by the radiometer (i.e., Special Sensor Microwave Imager), scatterometer (i.e., Quick Scatterometer and Advanced Scatterometer) and the Regional Atmospheric Circulation Model (RACMO2) based on categorical triple collocation (CTC) which can identify the most accurate observation with unknown true values. The CTC fusion product was generated by adopting the best source for each pixel during 1999–2017. The cumulative liquid water volume simulated by RACMO2 has significantly declined (at the 99% confidence level) by 210 Gt decade⁻¹, while the decreasing trends in CTC-fused liquid water days (-1.18 days decade⁻¹) and cumulative wet surface (-1.69×10^6 days km² decade⁻¹) were not statistically significant. The significantly negative trend in eastern AP snow liquid water agreed well with the simultaneous cooling, and may be linked with the increased adjacent sea ice.

1. Introduction

The Antarctic ice shelves experience surface snowmelt every summer, leading to the occurrence of snow liquid water (OLW). As the northernmost and warmest part of the Antarctic continent (Rau et al., 2004), the Antarctic Peninsula (AP) produces about 66% of the total meltwater volume in the Antarctic (Barrand et al., 2013). Wet snowpacks absorb much more incident solar radiation than dry snowpacks due to the lower albedo (Steffen et al., 1993). Snow liquid water may even weaken the ice shelves, providing the conditions for their break-ups (Scambos et al., 2000; van den Broeke, 2005). In March 2002, a persistent anomalous atmospheric circulation resulted in extensive surface ponding on the Larsen B Ice Shelf. Meltwater transported heat into the crevasses, leading to the deepening of crevasses and hence the catastrophic collapse (van den Broeke, 2005). Therefore, snow liquid water on the AP is of great importance to the surface mass and energy balances, as well as to the stability of ice shelves (Abdalati and Steffen, 1997; Picard and Fily, 2006).

The AP has recorded one of the largest increases in air temperature (Tair) on the Earth since the 1950s to the end of last century (Turner

et al., 2014; Oliva et al., 2017), which is unprecedented over the last two millennia (Vaughan et al., 2003). As a consequence, the meltwater volume has nearly doubled from 1950 to 2000 (Vaughan, 2006). Summer snowmelt during 1981–2000 was at a level that is unprecedented over the past millennium according to the ice-core proxies (Abram et al., 2013). However, Tair in the AP has decreased since 1999 as a consequence of enhanced east-to-southeasterly cold winds due to circulation changes (Turner et al., 2016; Oliva et al., 2017). The AP surface OLW has increased associated with the positive trend in Tair during 1978–1991 (Ridley, 1993), and showed large inter-annual variability during 1999–2009 (Barrand et al., 2013). Recent studies found a negative trend in OLW on the Larsen C Ice Shelf during 1999–2017 (Scott et al., 2018; Bevan et al., 2018).

Spaceborne microwave sensors can operate regardless of the weather and illumination conditions, and have been widely used to monitor snow and ice conditions in the polar regions where it is frequently cloudy and the in-situ measurements are sparse (Scott et al., 2017). The absorptivity and emissivity of microwave increase significantly when liquid water forms in the snowpacks (Ashcraft and Long, 2006; Liu et al., 2006), leading to the sudden increase of

* Corresponding author.

E-mail address: zhoucx@whu.edu.cn (C. Zhou).

<https://doi.org/10.1016/j.rse.2019.111219>

Received 17 December 2018; Received in revised form 13 May 2019; Accepted 26 May 2019

Available online 29 July 2019

0034-4257/ © 2019 Elsevier Inc. All rights reserved.

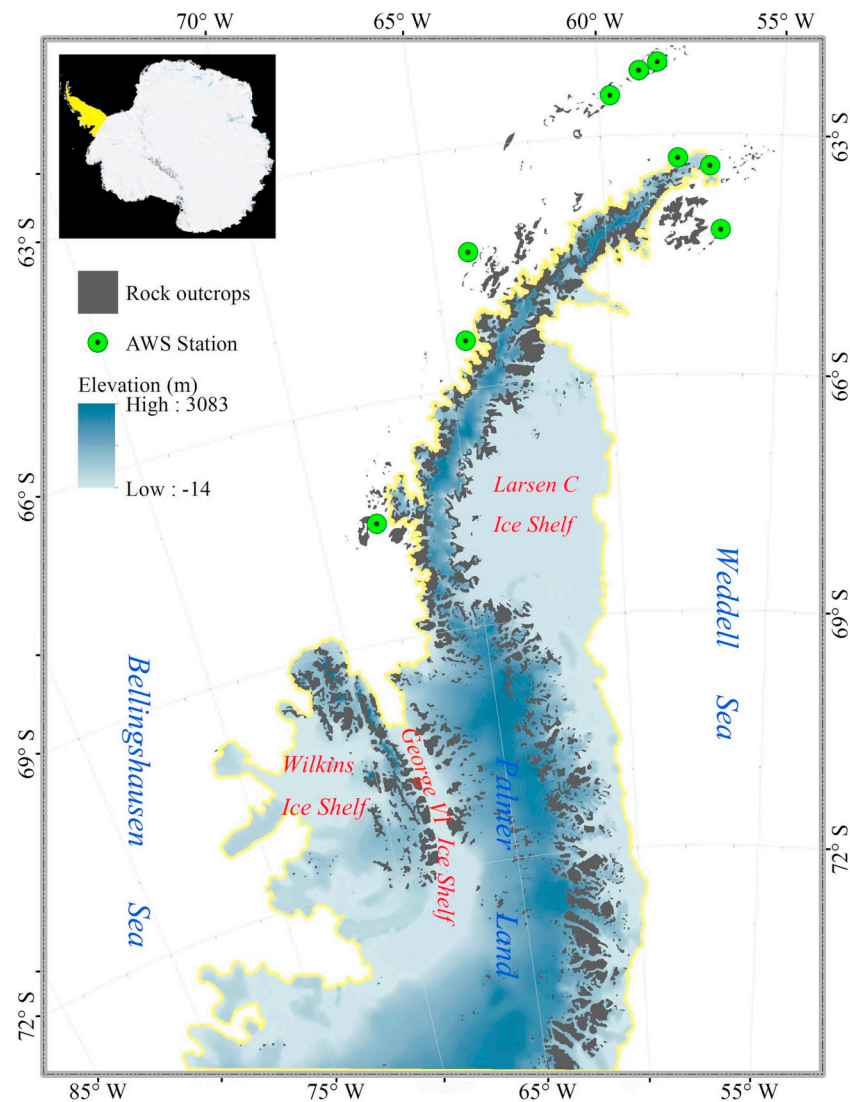


Fig. 1. Location (left top insert) and elevation of the AP. The Green dots represent the READER AWS stations (<https://legacy.bas.ac.uk/met/READER/>) listed in Table 1. The digital elevation model (DEM) (Bamber et al., 2009) and coastal lines (Scambos et al., 2007) of the AP were obtained from the National Snow and Ice Data Center (NSIDC, <http://nsidc.org/>). (For interpretation of the references to colour in this figure legend, the reader is referred to the web version of this article.)

brightness temperature (T_b) and the decrease of backscattering coefficient (σ^0). Microwave radiometers and scatterometers, such as the Scanning Multi-channel Microwave Radiometer (SMMR), Special Sensor Microwave Imager (SSM/I), Advanced Microwave Scanning Radiometer-Earth Observing System (AMSR-E), Quick Scatterometer (QSCAT) and Advanced Scatterometer (ASCAT) have been used to map wet snow over the ice sheets. Various models have been developed to investigate the evolution of liquid water in snowpacks in more detail. The Regional Atmospheric Circulation Model (RACMO2) even provides a time series of melt flux and liquid water content (LWC) over the ice sheets (van den Broeke et al., 2006; Kuipers Munneke et al., 2012).

However, significant discrepancies have been found in the wet snow mapped by these measurements. The various operating frequencies and the local acquisition time result in great differences in OLW detected by satellites (Ashcraft and Long, 2006; Picard and Fily, 2006; Tedesco, 2007). Scatterometer has been proved to be more sensitive to OLW than radiometer (Tedesco, 2007). However, the scatterometer is also sensitive to the surface roughness and morphological changes (Fraser et al., 2016; Wang et al., 2018) and may fail to detect OLW in the bare ice area where surface reflectivity dominates the backscatter (Zhou et al., 2019). Satellite-based observations can only give the presences or absences of the snow liquid water. The fast-changing snow properties make it

challenging to fathom the localized LWC quantitatively based on satellites. Models can simulate melt flux and LWC. However, the reliability of simulations relies heavily on the accuracy and resolution of the forcing data, which are always difficult to satisfy in polar regions. Moreover, some surface processes have not been fully described in the models. For the places influenced by coastal climate and föhn winds, RACMO2 shows local discrepancies in the reproduced OLW compared with satellite-based observations (Barrand et al., 2013; Trusel et al., 2013).

OLW detected by satellites has been evaluated against the positive Tair from the automatic weather stations (AWS) (e.g., Tedesco, 2009; Trusel et al., 2012; Liang et al., 2013; Steiner and Tedesco, 2014). However, Tair above the freezing point does not necessarily indicate the OLW in snowpack. Solar radiation penetration in the low thermal conductivity snowpack can result in subsurface snowmelt even when Tair is below the freezing point (Koh and Jordan, 1995). Suffering from the lack of in-situ snow wetness measurements, the relative performances of OLW products derived by the radiometer, scatterometer and model have never been evaluated. Stoffelen (1998) proposed a technique named triple collocation (TC) for the validation of measurement systems with respect to the unknown true values. TC is now widely used in estimating the errors in various measurements, such as soil moisture,

precipitation, snow depth, surface temperature, wind speed and leaf area index (Caires and Sterl, 2003; O'Carroll et al., 2008; Fang et al., 2012; Roebeling et al., 2012; Su et al., 2014; Xu and Shu, 2015; Gruber et al., 2017). For the wet/dry snow retrievals, however, the binary variables with only two elements suggest non-negligible correlations between the errors and the target variable, which violates the key assumptions of classical TC (Stoffelen, 1998). McColl et al. (2016) introduced a variant of Triple Collocation that can be applied to categorical target variables. The three different measurement systems are assumed to be conditionally independent, and their relative performances can be ranked by decomposing the sample covariance matrix. The Categorical Triple Collocation (CTC) can identify the most accurate one at a particular location with unknown true value.

Considering the recent cooling in the AP, this study aims at investigating the variations in snow liquid water based on merging satellite and model estimations. More specifically, our objectives of this paper are to: (i) rank the performances of radiometer (SSM/I), scatterometer (QSCAT and ASCAT) and climate model (RACMO2) in OLW estimation using CTC; (ii) describe the distribution patterns of OLW based on the fusion of optimal observations; and (iii) investigate the snow liquid water variations in the context of the cooling AP. This paper is organized as follows. Section 2 provides a brief introduction to the AP and the data set. Section 3 describes the methods for OLW detection and recalls the CTC algorithm developed by McColl et al. (2016). Section 4 presents the performance rankings in OLW detection, as well as the average and trend analyses. In Section 5, the main results are discussed, followed by the conclusion in Section 6.

2. Study area and data set

2.1. Study area

The AP is a northward extension of Antarctica towards the southern tip of South America with an average elevation of about 1500 m (Fig. 1). The mountains extend towards the Drake Passage, reaching 63° S. As the biggest and most prominent peninsula in Antarctica, the AP is ice-covered and mountainous, with long melt seasons (Fahnestock et al., 2002). The AP is sensitive to climate change and is undergoing rapid change, which is evident in the acceleration and thinning of glaciers (Rignot et al., 2013), retreat of glacier fronts (Cook et al., 2005) and break-up of ice shelves (Scambos et al., 2000; Massom et al., 2018). After the break-up of the Wordie, Wilkins and George VI Ice Shelves since the 1980s in the western AP, the eastern side of the AP has witnessed a rapid sequence of disintegration events on the Larsen B and Larsen C Ice Shelves in the 21st century (Scambos et al., 2000; Rau et al., 2004; Hogg and Gudmundsson, 2017).

2.2. Satellite observations

Carried aboard the Defense Meteorological Satellite Program (DMSP) satellites, since 1987, SSM/I has been used to study OLW on the ice sheets for > 30 years (Steffen et al., 1993; Fettweis et al., 2007; Tedesco and Monaghan, 2009; Steiner and Tedesco, 2014). We obtained the Level-3 Southern Hemisphere EASE-Grid Brightness Temperature data set from the National Snow and Ice Data Center (NSIDC, <http://nsidc.org/>). The daily T_b in both ascending and descending orbits spans from 1987 to present with a spatial resolution of 25 km. We utilized both passes of SSM/I horizontally polarized 19.35 GHz T_b to determine surface OLW.

QSCAT was a quick recovery mission to replace the NASA Scatterometer. Using a conically scanning antenna at Ku-band (13.4 GHz), QSCAT yielded a 90% daily global coverage (Tsai et al., 2000). QSCAT ceased operation in 2009, ASCAT was always used to extend the QSCAT backscatter record for the studies of OLW (Mortin et al., 2014; Kuipers Munneke et al., 2018). ASCAT is a C-band (5.3 GHz) scatterometer with three vertically polarized antennas for the

Exploitation of Meteorological Satellites (EUMETSAT) MetOp-A and MetOp-B. To improve the utility of the data, the Scatterometer Image Reconstruction (SIR) product has been developed by the NASA Scatterometer Climate Record Pathfinder (SCP) project (Long et al., 1993). The radar scatterometer-based data time series achieve a balance between resolution and coverage in the polar regions and are publicly available (<http://www.scp.byu.edu/>). We utilized the daily SIR product to recognize OLW with a nominal pixel spacing of 4.45 km for both QSCAT and ASCAT.

2.3. Air temperature measurements

The 2 m Tair obtained from the gridded ERA-Interim reanalysis is used to examine the climatology over the AP. ERA-Interim is a global reanalysis based on an atmospheric model and an assimilation system, which were produced by the European Centre for Medium-Range Weather Forecasts (ECMWF) and are considered to be the most reliable reanalysis in the Antarctic (Bracegirdle and Marshall, 2012). The data set provide a global view that encompasses many essential climate variables in a physically consistent framework, including the weather, ocean and land-surface conditions since 1979 (Dee et al., 2011).

Turner et al. (2016) and Oliva et al. (2017) found the AP cooling based on the AWS monthly Tair obtained from the Reference Antarctic Data for Environmental Research (READER) database (Turner et al., 2004), which was also used in this study. The AWS stations included in this work are illustrated in Fig. 1 and listed in Table 1. The AWS meteorological measurements were also used to depict the AP climate, and to validate the ERA-Interim reanalysis. The root mean square error (RMSE), bias and correlation coefficient between monthly ERA-Interim Tair and AWS Tair were 1.51 °C, 0.19 °C and 0.94 respectively (Fig. 2), suggesting the ERA-Interim reanalysis is a reliable dataset to examine the AP climate.

2.4. Regional climate model simulations

Forced by the ERA-Interim reanalysis, RACMO2 combines the atmospheric dynamics description from the High Resolution Limited Area Model (HIRLAM) with the physical processes from the ECMWF global model (van den Broeke et al., 2006). RACMO2 has been widely used to the studies in surface mass balance in the Antarctic, such as the melt flux, snowdrift, precipitation, sublimation, etc. (van den Broeke et al., 2006; Barrand et al., 2013; Trusel et al., 2013; Lenaerts et al., 2016). The satellite observations were compared with the 27.5 km RACMO2 melt flux and LWC.

3. Method

3.1. OLW detection methods

OLW from SSM/I, QSCAT and ASCAT is based on thresholding the T_b and σ^0 time series. Wet snow was determined when the daily

Table 1
AWS stations (green points in Fig. 1) examined in this research.

Station	Latitude (°)	Longitude (°)	Elevation (m)
Arturo Prat	−62.5	−59.7	5
Bellingshausen	−62.2	−58.9	16
Esperanza	−63.4	−57	13
Faraday/Vernadsky	−65.4	−64.4	11
Ferraz	−62.1	−58.4	20
Marambio	−64.2	−56.7	198
Marsh	−62.2	−58.9	10
O'Higgins	−63.3	−57.9	10
Orcadas	−60.7	−44.7	6
Palmer	−64.3	−64	8
Rothera	−67.5	−68.1	32

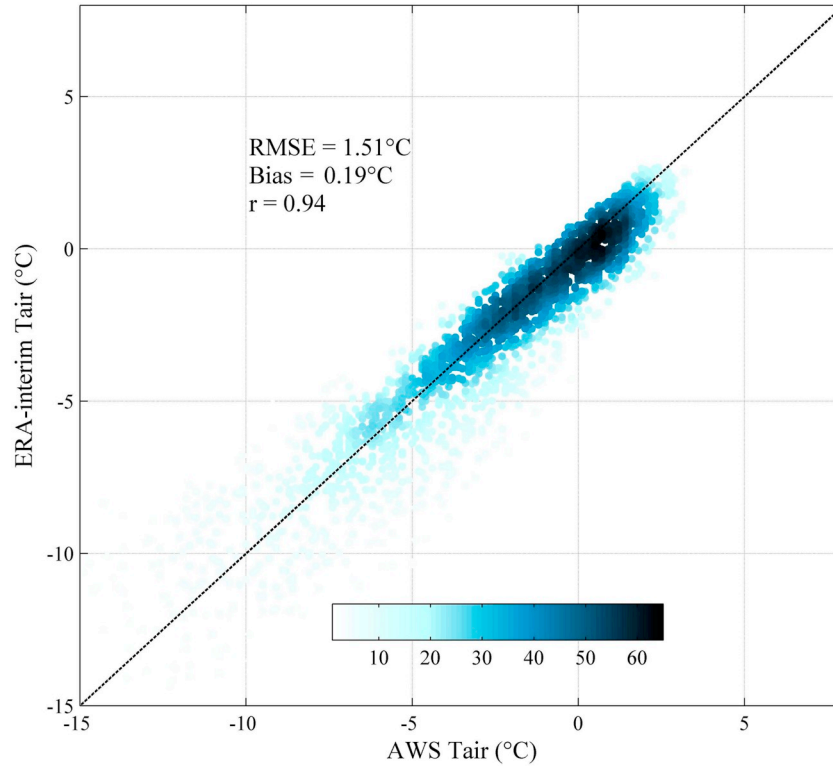


Fig. 2. Density scatter plot showing the comparison between AWS Tair and ERA-Interim Tair.

observations rise above (or drop below) a certain value. The general methods can be described as follows:

$$M(t) = \begin{cases} 1, T_b \geq T_{wm} + a \\ -1, T_b < T_{wm} + a \end{cases} \quad \text{for SSM/I, and} \\ = \begin{cases} 1, \sigma^0 \leq \sigma_{wm}^0 - b \\ -1, \sigma^0 > \sigma_{wm}^0 - b \end{cases} \quad \text{for QSCAT and ASCAT} \quad (1)$$

where t is time, $M(t)$ represents the wet/dry state with $M = 1$ indicating wet snow and $M = -1$ indicating dry snow. For SSM/I, we utilized the horizontally polarized 19 GHz T_b to recognize OLW, and T_{wm} is the winter (from May to July) mean T_b . OLW detected by this method agreed well with the positive Tair when a is set as 30 K (Zwally and Fiegles, 1994; Tedesco, 2009). Both the ascending and descending SSM/I passes were used in OLW detection. OLW was determined if any pass exceeds the corresponding threshold. For QSCAT, $b = 2$ dB was empirically determined by comparing with the Tair. However, a single threshold of 2 dB below the σ_{wm}^0 (i.e. winter mean σ^0) may cause misidentifications given that the Ku band σ^0 may decrease due to snow accumulation (Trusel et al., 2012). Thus, a dual threshold approach was conducted for early and late melt season. We refer to Trusel et al. (2012) for a detailed description of this methodology. The threshold for ASCAT was set as 2.7 dB according to Kuipers Munneke et al. (2018).

It is worthwhile to mention that OLW does not necessarily indicate snowmelt. Former studies often mistake the OLW determined by satellites for snowmelt. LWC and melt flux can be very different during the slight or intense melt season, which can be clearly seen in the comparison between satellite observations, simulated LWC and melt flux on the George VI Ice Shelf (71.90° S, 68.05° W) (Fig. 3). Meltwater refreezed quasi-instantaneously during slight snowmelt (van den Broeke et al., 2010) so that no liquid water remained in the snowpack within the model time step (see the black arrows in Fig. 3). In January, the magnitude of LWC was significantly higher than melt flux. Plenty of liquid water remained even when there was no snowmelt. Causes for these differences include two aspects. First, it takes time for meltwater

to refreeze after intense melt events. Second, subsurface liquid water may remain after the refreezing of the surface. σ^0 and T_b kept well below or above the thresholds due to the penetrating ability of microwave, and OLW was still detected by the satellites (Ashcraft and Long, 2006). Therefore, we compared OLW derived from satellites with that determined by LWC rather than melt flux. The RACMO2 OLW was determined when LWC is above 0.4 mm (i.e., 0.4 kg m⁻²) according to Barrand et al. (2013).

The liquid water days (LWD, the number of days with OLW), cumulative wet surface (CWS, the number of LWD times the area with wet snow) and liquid water intensity (LWI) were used to study the inter-annual variability in snow liquid water on the AP. CWS, also called melt index in Zwally and Fiegles (1994), is defined as the summing of the wet surface in a given year:

$$CWS = \sum_i^n \sum_j^m LWD_{i,j} S \quad (2)$$

where S is the pixel area for the $n \times m$ LWD matrix, i and j indicate the row and column for the grids. The unit for CWS is days km².

An approximately linear relationship has been documented between radar backscatter and snow LWC (Stiles and Ulaby, 1980), as well as melt flux (Trusel et al., 2013). LWI, also called melt intensity in Smith (2003) and melting decibel-days in Trusel et al. (2012), is calculated by summing up the reductions in radar backscatter over a certain time interval. Liquid water increases the microwave emissivity of snowpack, hence causing a sudden and significant increase in T_b (Hallikainen et al., 1986; Tedesco, 2009). Similarly, we also summed up the increases in SSM/I T_b to obtain LWI for radiometer. For the satellite-based observations, LWI is computed as:

$$LWI(y) = \sum_{1\text{July},y}^{30\text{June},y+1} \frac{1}{2} (M(t) + 1) (T_b(t) - T_{wm}) \quad \text{for SSM/I, and} \\ = \sum_{1\text{July},y}^{30\text{June},y+1} \frac{1}{2} (M(t) + 1) (\sigma_{wm}^0 - \sigma^0(t)) \quad \text{for QSCAT and ASCAT} \quad (3)$$

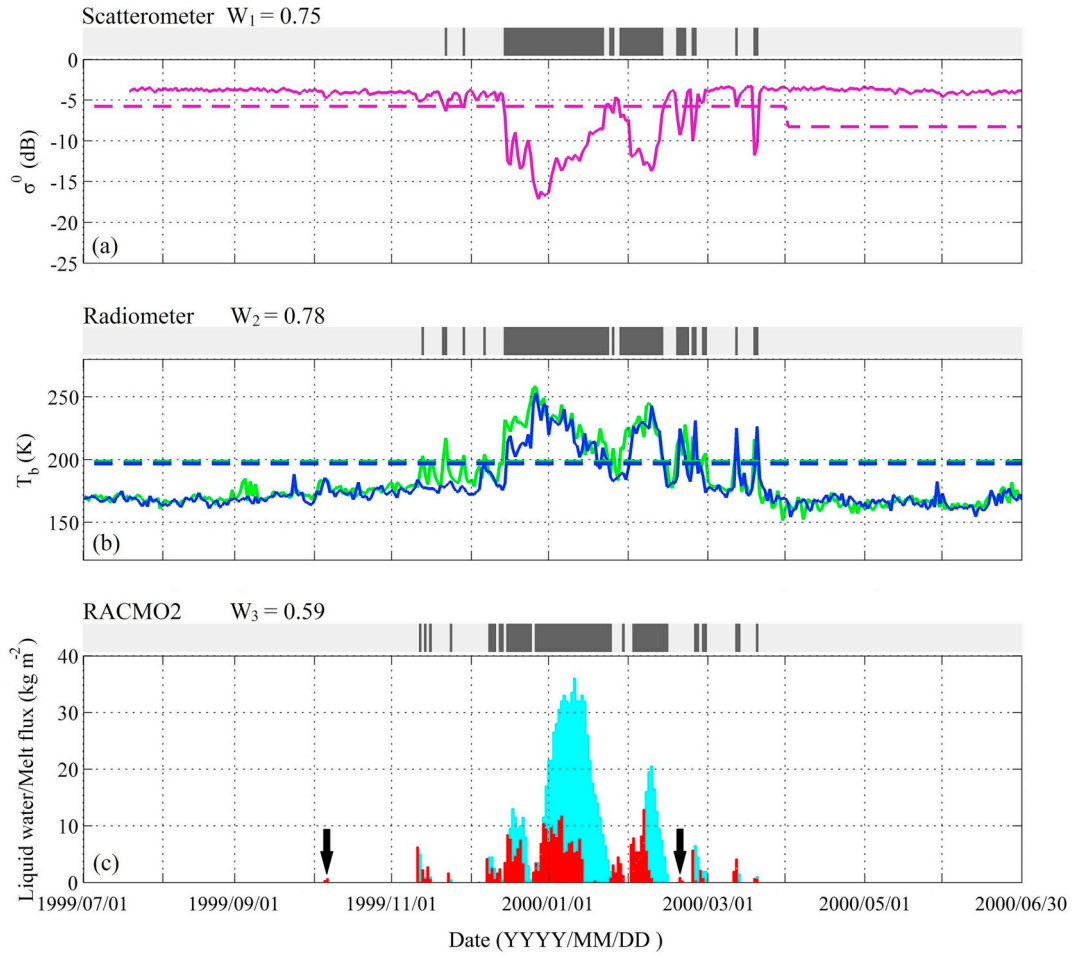


Fig. 3. Comparison of (a) QSCAT σ^0 (purple solid line), (b) SSM/I vertically polarized 19 GHz T_b in ascending (green solid line) and descending (blue solid line) passes, and (c) RACMO2 LWC (cyan bars) and melt flux (red bars) on the George VI Ice Shelf (71.90° S, 68.05° W) during 1999/2000. Dash lines are the thresholds for the measurements in corresponding colors. LWC > 0.4 kg m^{-2} is determined as OLW according to [Barrand et al. \(2013\)](#). Black arrows suggest snowmelt with quasi-instantaneously refrozen liquid water. Bars on the top of each measurement are the corresponding OLW detection with gray indicating absence and black indicating presence. (For interpretation of the references to colour in this figure legend, the reader is referred to the web version of this article.)

Units for LWI derived from radiometer and scatterometer are K days and dB days respectively. LWI can be an index for snow liquid water with the presumption that a larger volume of liquid water is manifested as greater reductions in radar backscatter and greater increases in T_b over the same time interval. LWI derived by the scatterometers shows strong and positive relations with positive Tair in the Antarctic and the Arctic ice caps ([Smith, 2003](#); [Trusel et al., 2012](#)).

3.2. Categorical triple collocation

It is difficult to evaluate the OLW derived from satellites and RACMO2 due to the lacking of snow wetness measurements. TC is a general solution to validate the measurements with unknown true values by assuming that the measurements (M) are related to the true values (T) as follows ([Stoffelen, 1998](#)):

$$M_i = A_i + B_i T + \varepsilon_i \quad (4)$$

where i represents the different measurement systems, A_i and B_i are calibration parameters. ε indicates the random error which can be estimated by assuming that errors of the measurement systems must be uncorrelated with each other and with the true value (e.g., [Roebeling et al., 2012](#); [Gruber et al., 2017](#)). For the binary wet/dry snow retrievals with only two values (1 and -1), Eq. (4) can be rewritten as ([McColl et al., 2016](#)):

$$M_i = T + \varepsilon_i \quad (5)$$

ε only has three possibilities: 0 indicates the observation is correct, 2 indicates dry snow is mistaken for wet snow, and -2 indicates wet snow is mistaken for dry snow. Obviously, ε is correlated with T for the binary retrievals, which violates the key assumption of classical TC.

Instead, the balanced accuracy (α) of measurement systems was introduced to measure the relative performances of the binary classifiers and correlate the errors and truth ([Parisi et al., 2014](#); [McColl et al., 2016](#)):

$$\alpha_i = \frac{1}{2}(\psi_i + \eta_i) \quad (6)$$

where ψ and η are the sensitivity (the probability of the measurement is true when it is wet snow) and specificity (the probability of the measurement is true when it is dry snow).

[Parisi et al. \(2014\)](#) showed that the sample covariance matrix (Q) corresponds to the balanced accuracy α for the stationary variables:

$$Q_{ij} \equiv \text{Cov}(M_i, M_j) = \begin{cases} 1 - E(E(M_i))^2, & \text{for } i = j \\ \text{Var}(T)(2\alpha_i - 1)(2\alpha_j - 1), & \text{for } i \neq j \end{cases} \quad (7)$$

Under standard assumptions of independence between the errors of each system, the performances of different measurement systems can be ranked with unknown error-free true values. We refer the readers to Appendix 1 of [Parisi et al. \(2014\)](#) for detailed derivations.

[McColl et al. \(2016\)](#) generalized the relation between covariance matrix (Q) and the balanced accuracy α to the non-stationary variables

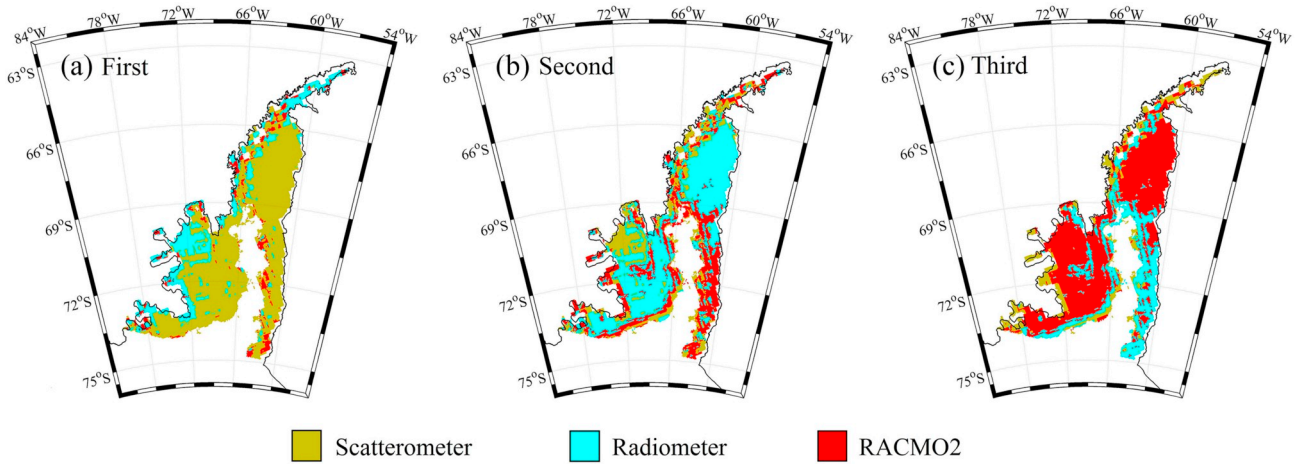


Fig. 4. Rankings of OLW derived by scatterometer (yellow), radiometer (cyan) and RACMO2 (red). (a), (b) and (c) present the measurements that rank the first, second and third. (For interpretation of the references to colour in this figure legend, the reader is referred to the web version of this article.)

which show significantly seasonal variations (e.g., the wet/dry snow retrievals):

$$Q_{ij} \equiv \text{Cov}(M_i, M_j) = \begin{cases} 1 - E(E(M_i/t))^2, & \text{for } i = j \\ 4E(p(t))(1 - E(p(t)))(2\alpha_i - 1)(2\alpha_j - 1), & \text{for } i \neq j \end{cases} \quad (8)$$

where $p(t) \equiv p_M (M = 1|t)$ and t is time. Random error ε for different measurement systems is supposed to be conditionally independent of each other when applying CTC (i.e., $\Pr(\varepsilon_i, \varepsilon_j|T) = \Pr(\varepsilon_i|T)\Pr(\varepsilon_j|T)$ for all $i \neq j$). We refer the readers to Appendix C of [McColl et al. \(2016\)](#) for detailed derivations. There are three equations for the three measurements systems when $i \neq j$. So if we define:

$$\mathbf{W}_i = 2(2\alpha_i - 1)\sqrt{E(p(t))(1 - E(p(t)))} \quad (9)$$

then we have:

$$\mathbf{W} = \begin{bmatrix} \sqrt{\frac{Q_{12}Q_{13}}{Q_{23}}} \\ \sqrt{\frac{Q_{12}Q_{23}}{Q_{13}}} \\ \sqrt{\frac{Q_{23}Q_{13}}{Q_{12}}} \end{bmatrix} \quad (10)$$

Since \mathbf{W}_i is a monotonic increasing function of α_i , the sorting of \mathbf{W} in descending order represents the rankings of the performance for the corresponding measurement system. CTC requires a less restrictive assumption to evaluate the relative accuracy of different measurement systems compared with TC. However, unlike the classical TC, CTC is not able to estimate the accurate error.

CTC has been employed to evaluate the landscape freeze/thaw state derived from in-situ air/soil temperatures, satellite and model estimations ([McColl et al., 2016](#); [Lyu et al., 2017](#)). Surprisingly, the in-situ measurements often display the poorest performance. Freeze/thaw or wet/dry retrievals are always heterogeneous spatially (e.g., due to variations in land cover and topography). These differences can be thought of as errors in the in-situ estimate (i.e., representativeness errors) ([Lyu et al., 2017](#)). CTC is valuable in the evaluation of binary estimations, rather than treating the weather station observations as an error-free truth ([McColl et al., 2016](#)).

Assuming conditional independence between the three different measurement systems, the 3×3 covariance matrix can be decomposed to estimate the rankings of OLW products with respect to their balanced accuracies. The ranking of OLW products based on CTC algorithm can be summarized as follows: (i) calculating the covariance matrix Q from

the scatterometer, radiometer and RACMO2 OLW estimations; (ii) estimating \mathbf{W} from Q based on Eq. (10); and (iii) obtaining the rankings by sorting \mathbf{W} in descending order. An example of the application of CTC is presented in [Fig. 3](#). \mathbf{W} for the scatterometer, radiometer and RACMO2 measurements was 0.75, 0.78 and 0.59 respectively, suggesting that radiometer ranked the first in this site, followed by the scatterometer, and RACMO2 exhibited the poorest performance. CTC was conducted over the AP during 1999–2017. A CTC fusion OLW product was generated by adopting the best source for each pixel.

3.3. Data preprocessing and analysis

We examined the AP snow liquid water variations over the period 1999–2017. To capture continuous melt seasons, statistics for each year start on 1 July and end on 30 June in the following year. The missing satellite observations were filled based on time-line interpolation. SSM/I grids (25 km) and RACMO2 grids (27.5 km) were reprojected and resampled to the same spatial resolution as the scatterometer (4.45 km). Linear trends were derived using a least-squares adjustment. The significance levels of the correlations and regressions were determined using the Student's t -tests. The AWS Tair observations were occasionally missing. Only the stations with continuous measurements were examined in trend analysis, including the Bellingshausen, Esperanza, Faraday/Vernadsky, Marambio and Rothera Stations.

4. Results

4.1. Rankings in OLW detection

We evaluated the OLW derived by scatterometer, radiometer and RACMO2 based on CTC by sorting their performances ([Fig. 4](#)). Scatterometer ranked the first in OLW detection (70% of the cases) on most of the low-lying ice shelves ([Fig. 4a](#)). Radiometer showed the best performance (22% of the cases) in the coastal areas of western AP, the Wilkin Ice Shelf and the grounding zone of Larsen C Ice Shelf ([Fig. 4a](#)). RACMO2 ranked the highest in very limited places (8% of the cases), mainly distributed in the mountainous areas with rock outcrops in the Graham and Palmer Lands ([Fig. 4a](#)). Radiometer ranked the second in most of the AP, while RACMO2 ranked the second in the regions with considerable surface slopes ([Fig. 4b](#)). Radiometer showed the worst performance in OLW detection in mountainous areas. Though RACMO2 ranked the last in most of the AP ([Fig. 4c](#)), it showed good performance in the regions of complex topography where it is always difficult for satellites to work.

Not all the satellite-based OLW detection methods were compared.

Methods based on the cross-polarization gradient ratio (XPGR) and diurnal variations have also been used in OLW detection (Abdalati and Steffen, 1997; Fettweis et al., 2007; Tedesco, 2007). However, the XPGR algorithm may fail to work when the LWC is very low at high-latitudes (Tedesco, 2007). Methods based on diurnal changes of T_b or σ^0 may miss the OLW when liquid water does not refreeze or even melts at night (Zheng et al., 2018). Though the OLW detection methods used in this study have been found to be very sensitive to OLW and work well when compared with Tair (Tedesco, 2009; Trusel et al., 2012), the ideal thresholds may vary with different snow properties and stratification of the snowpacks (Liu et al., 2005; Ashcraft and Long, 2006). The C band ASCAT was always used to detect OLW after the QSCAT ceased operation (Mortin et al., 2014; Kuipers Munneke et al., 2018). However, the lower frequency measurements may be less sensitive to liquid water due to the less microwave absorption (Ashcraft and Long, 2006). RACMO2 simulates LWC for the whole snowpack, while satellite can only detect OLW above the penetration depth. RACMO2 OLW was determined based on the total daily LWC, while only one or two daily satellite observations were used in this study, potentially missing the OLW because melting and refreezing can occur in any time of the day (Zheng et al., 2018).

Snow wetness may vary in a limited area, especially for the regions of complex topography. The inconsistent spatial resolutions for the measurements may obscure performance rankings based on CTC (McColl et al., 2016). It is important to mention that CTC gives the performance rankings of wet/dry state retrievals rather than the error magnitudes. This is the price paid for relaxing two key assumptions of classical TC. The CTC fusion product is the combination of the best source for each pixel rather than the accurate measurements, possibly resulting in discontinuities in space. Nevertheless, CTC provides a promising method to merge the OLW estimations in the AP where reliable in-situ measurements are not available.

4.2. CTC fusion and OLW distribution

As illustrated above, the scatterometer, radiometer and RACMO2 presented complementary nature in OLW estimation. We generated a fusion product by adopting the best source identified by CTC for each pixel. OLW was only detected by scatterometer in some coastal areas where SSM/I and RACMO2 fail to work due to the coarse spatial resolutions. Vacancies in these places were filled with scatterometer measurements. The correlation coefficients between the daily wet snow extent and ERA-Interim daily mean Tair were 0.64, 0.64, 0.55 and 0.65 for scatterometer, radiometer, RACMO2 and CTC fusion product respectively. The CTC fusion product showed a slightly higher correlation with Tair than satellite and model measurements.

The daily mean wet snow extent variations suggest that wet snow on the AP began to expand in November. After reaching the peak ($1.93 \times 10^5 \text{ km}^2$ according to CTC fusion product, i.e., 46% of the AP) in January (the middle of austral summer), wet snow extent shrank quickly and the AP became almost totally frozen in April (Fig. 5). Winter OLW was recognized by all the measurements, which has been reported by a recent research (Kuipers Munneke et al., 2018). Wet snow extent derived by radiometer was the largest from November to January, and became the smallest in late melt season when scatterometer detected the most extensive OLW. Wet snow extent derived by RACMO2 was much smaller than that mapped by satellites. The wet snow extent based on CTC fusion product was closest to that derived by scatterometer.

Annual mean LWD derived by each measurement system is presented in Fig. 6. Generally, LWD decreased with the increasing elevations. OLW in the western AP occurred more frequently than that in the eastern AP. All the observations showed that the LWD can be > 100 days on the Wilkins Ice Shelf. Wet snow lasted for more than two months on the Larsen C, Wilkins and George VI Ice Shelves where LWD detected by satellites was significantly more than that derived by

RACMO2. Owing to the warming effect of the föhn winds, the most intense snowmelt and the highest LWD on the Larsen C Ice Shelf were always found in the grounding zone (Luckman et al., 2014; King et al., 2017). This phenomenon was successfully identified by the satellite-based and CTC fusion products, while RACMO2 failed to capture this local process.

4.3. Liquid water and snowmelt dynamic changes

Daily AP wet snow extent over 1999–2017 derived by each measurement is shown in Fig. 7. Extensive wet snow was found in 2002/2003 when about 30% of the AP did not refreeze in late March according to the CTC product. Both satellites and the RACMO2 estimations showed limited wet snow on the AP in 2013/2014. Generally, radiometer-based wet snow extent is larger than that derived by scatterometer and RACMO2 in austral summer. Wet snow mapped by radiometer shrank quickly after mid-February (Fig. 7b), while a large portion of the AP did not refreeze after March according to scatterometer, RACMO2 and CTC fusion measurements (Fig. 7a, c, d).

On average, CWS derived by CTC fusion product was $12.93 \times 10^6 \text{ days km}^2$ during 1999–2017 (Fig. 8 and Table 2). CTC-fused CWS reached the maximum in 2002/2003 ($18.83 \times 10^6 \text{ days km}^2$) and the minimum in 2013/2014 ($5.78 \times 10^6 \text{ days km}^2$). All the measurement systems revealed a decreasing trend in CWS, varying from $-0.28 \times 10^6 \text{ days km}^2 \text{ decade}^{-1}$ (RACMO2) to $-1.69 \times 10^6 \text{ days km}^2 \text{ decade}^{-1}$ (CTC fusion product). LWD derived by CTC fusion product also peaked in 2002/2003 and reached the lowest point in 2013/2014 (Fig. 8b). A negative trend in LWD was also found during 1999–2017, varying from $-0.23 \text{ days decade}^{-1}$ (RACMO2) to $-1.18 \text{ days decade}^{-1}$ (CTC fusion product). The decreasing trends in CTC-fused CWS ($-0.30 \times 10^6 \text{ days km}^2 \text{ decade}^{-1}$) and LWD ($-1.97 \text{ days decade}^{-1}$) were both significant above the 90% confidence level over 1999–2016. However, the trends over 1999–2017 were not significant anymore because CWS and LWD reached the second highest in 2016/2017 and the sudden level shifts can confound trend analysis (Weatherhead et al., 1998).

Similar to CWS, we summed up the cumulative LWI on the AP by multiplying the LWI with pixel area. Annual meltwater and liquid water volume were also calculated by summing the daily measurements. Strong positive correlations between the RACMO2 meltwater volume and the cumulative LWI derived from the satellites are indicated by high correlation coefficients, which were 0.66, 0.92 and 0.65 for SSM/I, QSCAT and ASCAT respectively (Fig. 9a). High correlations were also found between the RACMO2 liquid water volume and the cumulative LWI derived from SSM/I (0.61), QSCAT (0.82) and ASCAT (0.71), which were all significant above the 95% confidence level (Fig. 9b). These significant linear relationships suggest LWI can serve as a proxy indicator of snow liquid water.

The strong correlations between satellite-derived LWI and the simulated meltwater and liquid water volume are also evident in their consistent temporal variations (Fig. 10). On average, meltwater and liquid water volume were $44.76 \pm 11.68 \text{ Gt}$ and $795.95 \pm 181.97 \text{ Gt}$ (Table 3). The AP experienced intense surface snowmelt in 2002/2003 with the largest meltwater volume (70.46 Gt) and liquid water volume (1334.95 Gt), as well as the second highest SSM/I cumulative LWI. In 2013/2014, meltwater and liquid water volume were only 23.54 Gt and 524.21 Gt. Meanwhile, cumulative LWI reached the minimums. Cumulative LWI derived by QSCAT and ASCAT were calculated separately due to the different operating frequencies. SSM/I cumulative LWI and the meltwater volume presented negative trends during 1999–2017. The decreasing rate of liquid water volume ($-210 \text{ Gt decade}^{-1}$) was significant at the 99% confidence level over 1999–2017.

Most parts of the AP exhibited a negative trend in LWD since 1999 according to the CTC fusion product, especially for the Larsen C and George VI Ice Shelves (Fig. 11a). Remarkably, the decline of LWD in the southern Larsen C Ice Shelf was significant and can reach > 20 days

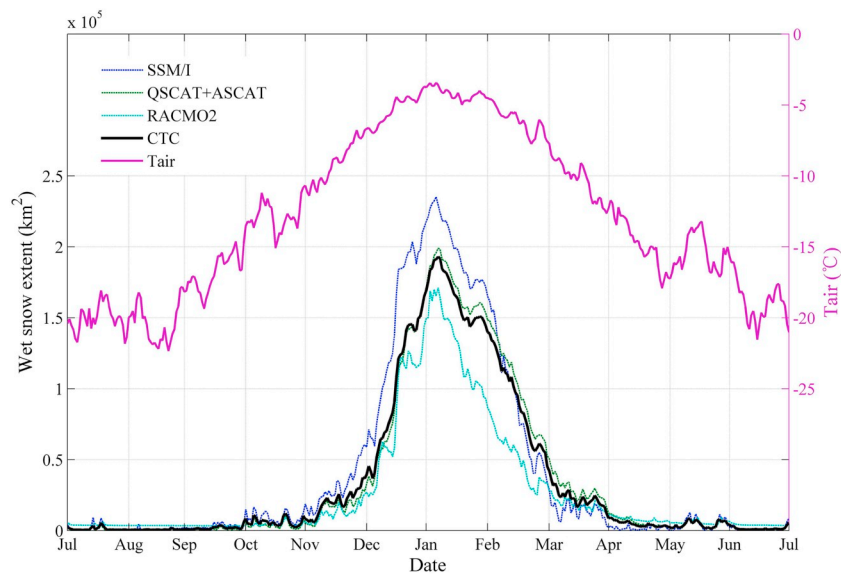


Fig. 5. Daily mean AP wet snow extent derived by scatterometer (green line), radiometer (blue line), RACMO2 (cyan line) and CTC (black line). Also shown is the ERA-Interim daily mean Tair (pink line) over the AP. (For interpretation of the references to colour in this figure legend, the reader is referred to the web version of this article.)

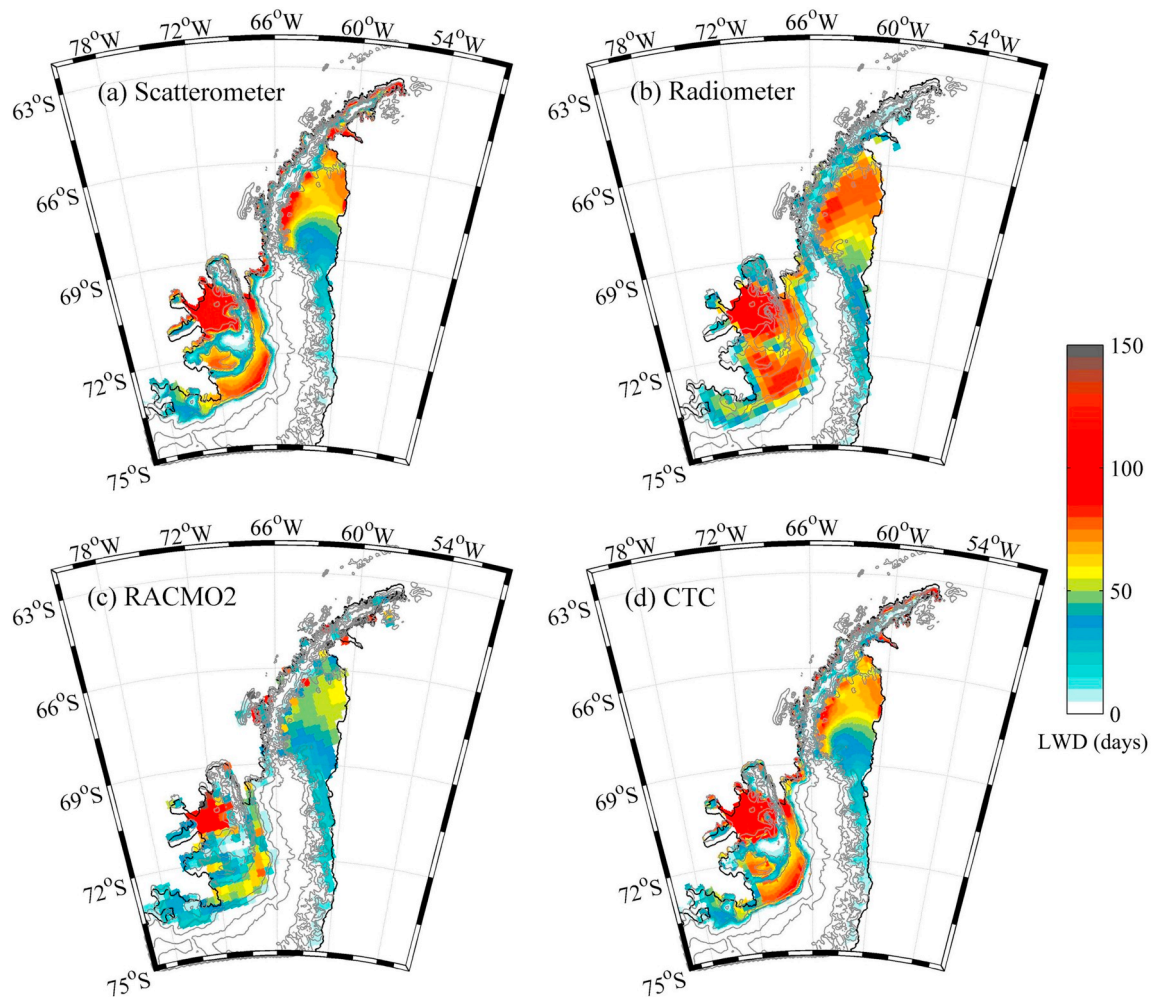


Fig. 6. Annual mean LWD based on (a) scatterometer, (b) radiometer, (c) RACMO2 and (d) CTC fusion product. Elevation contours are shown in gray.

decade⁻¹, which was consistent with the results from Bevan et al. (2018). The very limited increase of LWD was sporadically found in the western AP, mainly distributed along the coast. Previous studies have found interactions between ice sheet OLW and the adjacent sea ice variations through atmospheric circulation (Stroeve et al., 2017; Scott

et al., 2018). SIC has significantly increased in the adjacent seas of the AP over 1999–2017, especially in the Weddell Sea (Fig. 11b). The decreasing snow liquid water in the AP was in line with the simultaneous cooling over 1999–2017 revealed by both the ERA-Interim and AWS Tair measurements (Fig. 11c).

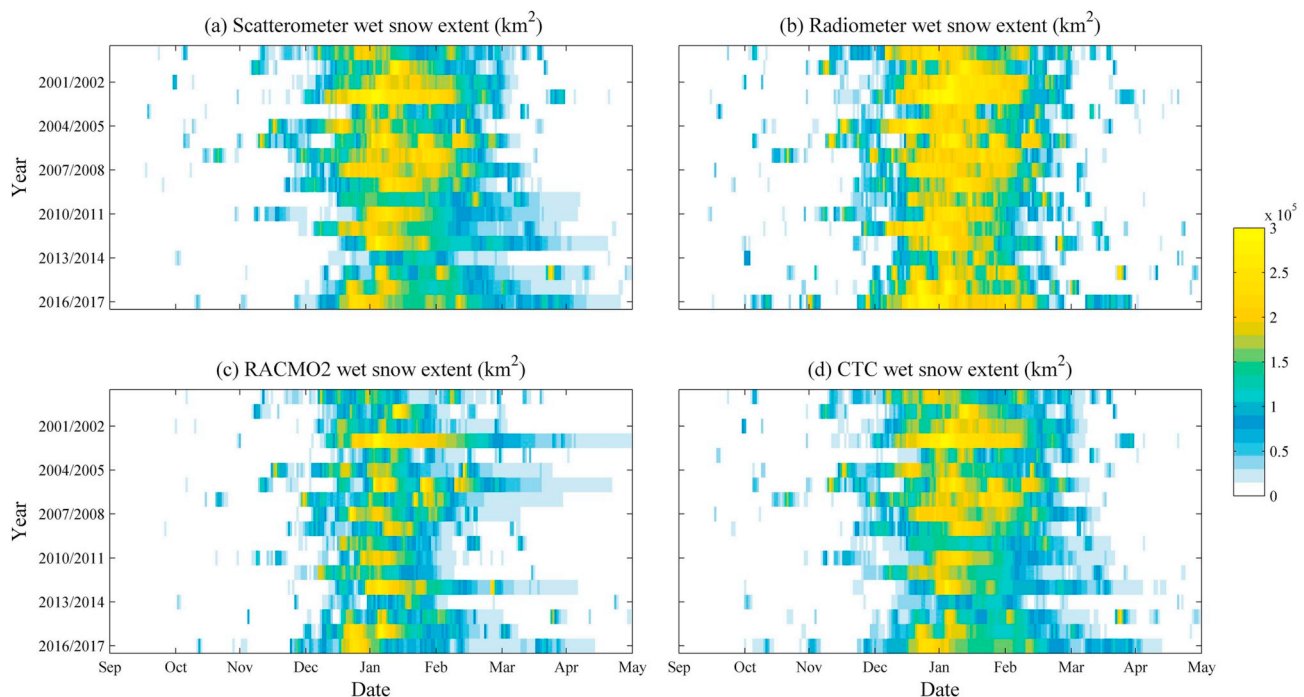


Fig. 7. Daily wet snow extent mapped by (a) scattermeter, (b) radiometer, (c) RACMO2 and (d) CTC fusion product during 1999–2017.

5. Discussion

5.1. Rankings in OLW detection

OLW detection based on satellite observations is related to snow wetness and the depth of the wet snow layer. It is not surprising that scattermeter ranked the first in most cases (70%) because active microwave measurements are extremely sensitive to OLW (Tedesco, 2007). Moreover, QSCAT and ASCAT operate in low frequencies, allowing for the recognition of deeper subsurface liquid water (Ashcraft and Long, 2006; Hall et al., 2009). Therefore more extensive wet snow was mapped by scattermeter compared with radiometer in late melt season (Fig. 5).

In the Greenland Ice Sheet, SSM/I was sensitive to OLW along the coast where normally heavy snowmelt occurs, while it was much less sensitive to the low LWC in the interior of Greenland (Tedesco, 2007).

Table 2

CWS and LWD statistics in the AP during 1999–2017.

Data set	Mean and std. dev. of CWS (10^6 days km^2)	CWS trend (10^6 days km^2 decade $^{-1}$)	LWD trend (days decade $^{-1}$)
Scattermeter	13.26 ± 3.15	-0.69	-0.49
Radiometer	15.33 ± 3.01	-0.81	-0.58
RACMO2	10.08 ± 3.18	-0.28	-0.23
CTC fusion product	12.93 ± 3.13	-1.65	-1.18

In a similar manner in the AP, SSM/I was also sensitive to OLW and ranked the first in the places where heavy snowmelt was found on the AP. In the western coast of the AP, the Wilkins Ice Shelf and the grounding zone of Larsen C Ice Shelf, LWD can last for more than two

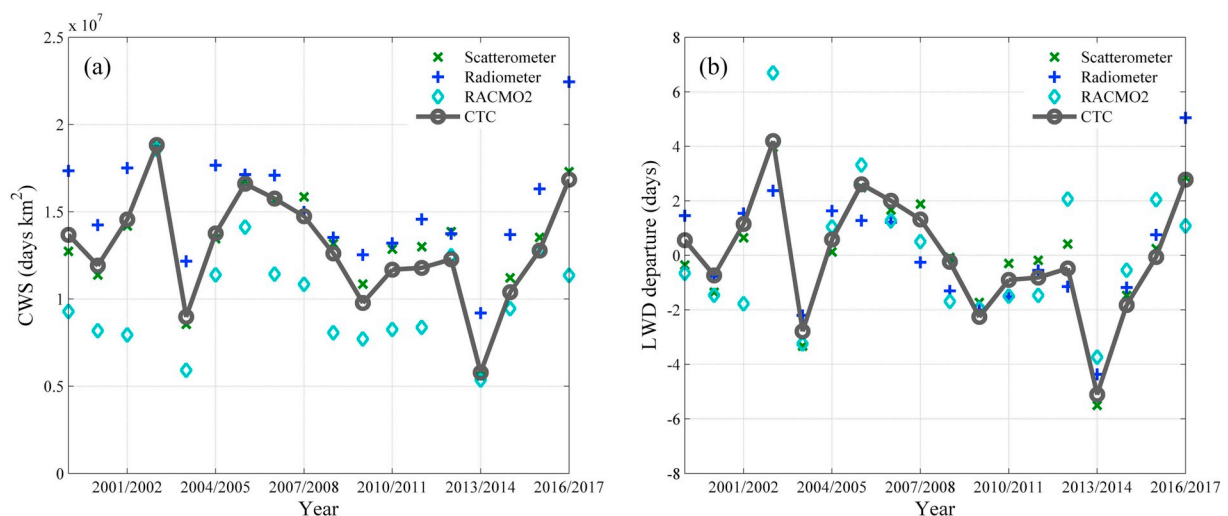


Fig. 8. (a) CWS and (b) LWD departure based on scattermeter (green crosses), radiometer (blue pluses), RACMO2 (cyan diamonds) and CTC-fused (black line) measurements during 1999–2017. (For interpretation of the references to colour in this figure legend, the reader is referred to the web version of this article.)

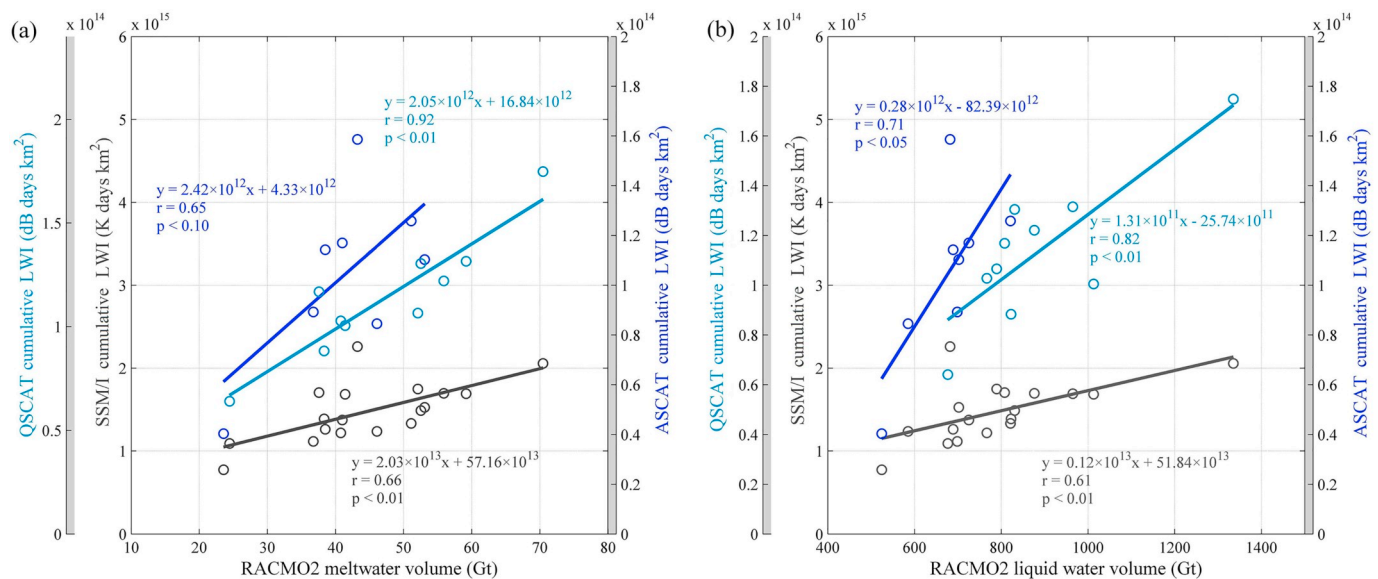


Fig. 9. Relationships between cumulative LWI derived from satellites and RACMO2 simulated (a) meltwater volume and (b) liquid water volume. Black, cyan and blue dots represent the SSM/I, QSCAT and ASCAT measurements respectively. Solid lines in the corresponding colors are the regression lines. (For interpretation of the references to colour in this figure legend, the reader is referred to the web version of this article.)

months, accompanied by the widespread of melt ponds and bare ice (Luckman et al., 2014; Zhou and Zheng, 2017). Dominated by specular reflection, radar backscatter from water and ice surface is generally weak and shows little variations in melt seasons (Fors et al., 2017; Zhou and Zheng, 2017), making it difficult for the scatterometers to detect OLW. While the OLW detection method based on SSM/I works well in intense melt season (Tedesco, 2009) and ranked the first in the regions with high LWD.

The intense snowmelt in the grounding zone of the Larsen C Ice Shelf results from the dry downslope föhn winds (Luckman et al., 2014). RACMO2 underestimated OLW along the coast and the grounding zone on the Larsen C Ice Shelf due to the crude representation of coastal climate and lack of föhn effects in the model (Barrand et al., 2013). Nevertheless, RACMO2 ranked the first in the mountainous areas with rock outcrops where it is difficult for satellites to work. Radar backscatter of rock is generally higher than the surrounding polar ice in the Antarctic (Fraser et al., 2014, 2016). Surface reflectivity dominates the radar backscatter from rocky surface, which is very

stable (Parajka et al., 2005) and can obscure the OLW signals. The specific heat capacity of rocks is much lower than that of ice and water. Thus rocky surface shows higher annual surface temperature and T_b variations, potentially resulting in the misidentifications of OLW based on radiometer (Zheng et al., 2018).

5.2. Climate forcing of the AP snow liquid water

AP Tair records showed significant warming trends (above 90% confidence level by Student's t -tests) since the 1950s to the end of the last century (Vaughan et al., 2003). However, the regional temperature record has shifted to a cooling trend since 1999, accompanied by a significant positive trend in sea ice concentration around the northern AP and the north Weddell Sea (Turner et al., 2016; Oliva et al., 2017).

The correlation between ice sheet OLW and the adjacent sea ice variations has been found in the western Greenland (Stroeve et al., 2017) and the West Antarctic (Scott et al., 2018). The declining sea ice resulted in increasing air-sea fluxes, leading to the increase of humidity

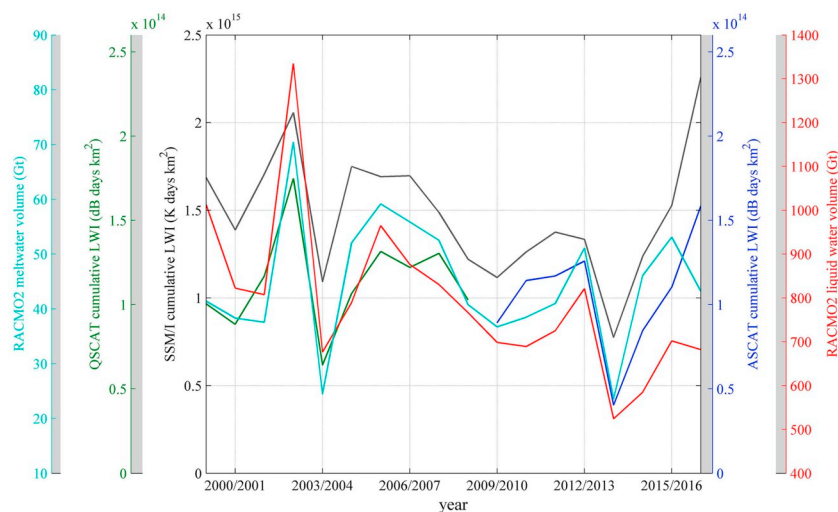


Fig. 10. Cumulative LWI derived by SSM/I (black line), QSCAT (green line) and ASCAT (blue line). The RACMO2 liquid water volume (red line) and meltwater volume (cyan line) are also shown. (For interpretation of the references to colour in this figure legend, the reader is referred to the web version of this article.)

Table 3

Cumulative LWI, liquid water and meltwater volume in the AP. * indicates the trend that is statistically significant at the 99% level.

Measurement	Mean and Std. dev.	Trend
SSM/I cumulative LWI (1999–2017)	$14.81 \pm 3.60 \times 10^{14}$ K days km ²	-1.34×10^{14} K days km ² decade ⁻¹
RACMO2 liquid water volume (1999–2017)	794.95 ± 180.97 Gt	-210.31 Gt decade ⁻¹ *
RACMO2 meltwater volume (1999–2017)	44.76 ± 11.68 Gt	-1.69 Gt decade ⁻¹
QSCAT cumulative LWI (1999–2008)	$11.38 \pm 2.96 \times 10^{13}$ dB days km ²	1.54×10^{13} dB days km ² decade ⁻¹
ASCAT cumulative LWI (2008–2017)	$10.50 \pm 3.47 \times 10^{13}$ dB days km ²	3.37×10^{13} dB days km ² decade ⁻¹

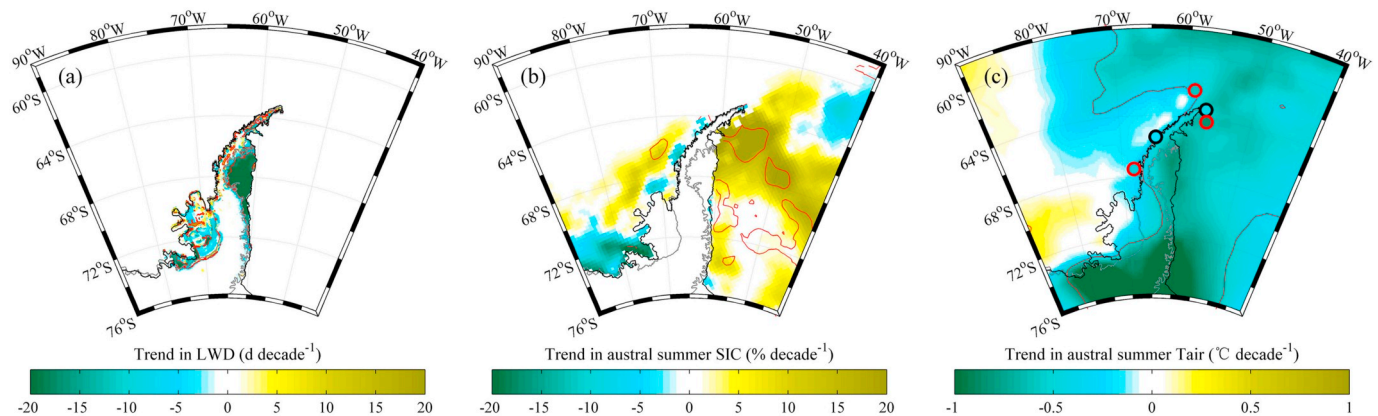


Fig. 11. Trends in (a) LWD, (b) sea ice concentration and (c) summer mean ERA-Interim Tair and AWS Tair (points) during 1999–2017. Red contours indicate the areas or stations significant at 90% confidence level. The Bootstrap sea ice concentration product was obtained from the NSIDC (<http://nsidc.org/data/nsidc-0079>) (Comiso, 2017). (For interpretation of the references to colour in this figure legend, the reader is referred to the web version of this article.)

and Tair over the Greenland Ice Sheet and enhancing surface snowmelt (Stroeve et al., 2017). The recently enhanced mid-latitude jet in the Weddell Sea resulted in stronger easterly and southeasterly near-surface flows towards the peninsula, pushing sea ice towards the AP's east coast. The reducing heat flux results in the cooling in the eastern AP (Turner et al., 2016; Steig, 2016). LWD in the eastern AP has declined considerably, especially on the Larsen C Ice Shelf, which has recently been reported by Bevan et al. (2018). The western AP Tair has also been found to be negatively correlated with the sea ice variations in the Amundsen-Bellinghshausen Seas (Jacobs and Comiso, 1997; Turner et al., 2013). We found a significant anti-correlation ($r = -0.43$, $p < 0.1$) between the CWS in the AP and the austral summer mean sea ice area in the Amundsen-Bellinghshausen-Weddell Seas (130°W–20°E).

The cooling trend in most of the western AP was insignificant. LWD along the coast of western AP and on some parts of the Wilkins Ice Shelf even slightly increased. This trend was attributed to the enhanced anticyclonic advection of marine air towards the coast of the West Antarctica (Scott et al., 2018). Prolonged snow liquid water in the western AP was found in 2016/2017 when LWD on the Wilkins Ice Shelf can be 50 days longer than the annual average (not shown) and the CTC-fused CWS and LWD in the AP were the second highest during 1999–2017 (Fig. 8). All the AWS stations with continuous Tair measurements in west AP have recorded an abnormal warming in 2016/2017, particularly at the Bellingshausen Station where the observed summer mean Tair was 1.23 °C higher than the previous year. ERA-Interim summer mean Tair of the AP reached the peak in 2016/2017, which was 0.84 °C higher than the annual average. Snow liquid water from satellite observations increased in 2016/2017, while that simulated by RACMO2 was lower than the previous year (Figs. 8 and 10). The decreasing trend in RACMO2 liquid water volume was even significant over 1999–2017. It is very likely that RACMO2 failed to simulate the increased snow liquid water in 2016/2017 considering its worst performance in OLW estimation and the sudden warming. Nevertheless, increased CWS and LWD in 2016/2017 were still revealed by CTC fusion product regardless of the interference from RACMO2 simulations.

6. Conclusion

We investigated the AP snow liquid water variations by merging satellite and model estimations in the context of the cooling AP during 1999–2017, and conclude that:

1. Scatterometer ranked the first in OLW detection in most of the AP because of its sensitivity to liquid water. Radiometer showed the best performance in the places with long melt seasons. RACMO2 was the most applicable in the mountainous areas with rock outcrops where it is difficult for the satellites to work. OLW derived from scatterometer, radiometer and RACMO2 showed complementary nature.
2. Cumulative LWI derived by satellites showed high correlations with the RACMO2 liquid water volume, which has been significant decreasing (at the 99% confidence level) at a rate of 210 Gt decade⁻¹. However, the decreasing trends in snow liquid water from satellite-based and CTC-fused products were statistically insignificant.
3. LWD on most of the Larsen C Ice Shelf has significantly decreased over 1999–2017, which agreed well with the simultaneous cooling, and may be linked with the increased adjacent sea ice.

Large-scale and continuous snow wetness measurements should be collected for the further validation of OLW detection. The decreasing OLW on the AP does not necessarily indicate a positive surface mass balance because most of the meltwater instantaneously refreezes in snowpacks. Climate model has projected the prospective intensification of surface snowmelt on the AP under both intermediate and high emissions scenarios in the rest of this century (Trusel et al., 2015).

Acknowledgements

We would like to thank the National Snow and Ice Data Center and the Brigham Young University for providing SSM/I, QSCAT and ASCAT data. We acknowledge Dr. Michiel van den Broeke for providing the RACMO2 simulations and the valuable discussions during this study.

We also thank Dr. Kaighin McColl for providing the consultation and codes of the CTC (<https://github.com/kaighin/CTC>). We are grateful to the three anonymous reviewers and the editorial team for their attention and time dedicated to this manuscript and for their constructive comments. The numerical calculations in this paper have been done on the supercomputing system in the Supercomputing Center of Wuhan University. This research was supported by the National Natural Science Foundation of China (NSFC) (Grant Nos. 41776200, 41531069, 41376187) and the National Key Research and Development Program of China (Grant No. 2018YFC1406102).

References

- Abdalati, W., Steffen, K., 1997. Snowmelt on the Greenland Ice Sheet as derived from passive microwave satellite data. *J. Clim.* 10 (2), 165–175. [https://doi.org/10.1175/1520-0442\(1997\)010<0165:SOTGIS>2.0.CO;2](https://doi.org/10.1175/1520-0442(1997)010<0165:SOTGIS>2.0.CO;2).
- Abram, N.J., Mulvaney, R., Wolff, E.W., Triest, J., Kipfstuhl, S., Trusel, L.D., Vimeux, F., Fleet, L., Arrowsmith, C., 2013. Acceleration of snow melt in an Antarctic Peninsula ice core during the twentieth century. *Nat. Geosci.* 6 (5), 404–411. <https://doi.org/10.1038/ngeo1787>.
- Ashcraft, I.S., Long, D.G., 2006. Comparison of methods for melt detection over Greenland using active and passive microwave measurements. *Int. J. Remote Sens.* 27 (12), 2469–2488. <https://doi.org/10.1080/01431160500534465>.
- Bamber, J.L., Gomez-Dans, J.L., Griggs, J.A., 2009. A new 1 km digital elevation model of the Antarctic derived from combined satellite radar and laser data – part 1: data and methods. *Cryosphere* 3 (1), 101–111.
- Barrand, N.E., Vaughan, D.G., Steiner, N., Tedesco, M., Kuipers Munneke, P., van den Broeke, M.R., Hosking, J.S., 2013. Trends in Antarctic Peninsula surface melting conditions from observations and regional climate modeling. *J. Geophys. Res. Earth Surf.* 118 (1), 315–330. <https://doi.org/10.1029/2012JF002559>.
- Bevan, S.L., Luckman, A.J., Kuipers Munneke, P., Hubbard, B., Kullessa, B., Ashmore, D.W., 2018. Decline in surface melt duration on Larsen C Ice Shelf revealed by the Advanced Scatterometer (ASCAT). *Earth Space Sci.* 5 (10), 578–591. <https://doi.org/10.1029/2018EA000421>.
- Bracegirdle, T.J., Marshall, G.J., 2012. The reliability of Antarctic tropospheric pressure and temperature in the latest global reanalyses. *J. Clim.* 25 (20), 7138–7146. <https://doi.org/10.1175/JCLI-D-11-00685.1>.
- Caires, S., Sterl, A., 2003. Validation of ocean wind and wave data using triple collocation. *J. Geophys. Res.* 108 (C3), 3098. <https://doi.org/10.1029/2002JC001491>.
- Comiso, J., 2017. Bootstrap Sea Ice Concentrations From Nimbus-7 SMMR and DMSP SSM/I-SSMIS, Version 3. NASA National Snow and Ice Data Center Distributed Active Archive Center. NSIDC. <https://doi.org/10.5067/7Q8HCCWS4I0R>.
- Cook, A.J., Fox, A.J., Vaughan, D.G., Ferrigno, J.G., 2005. Retreating glacier fronts on the Antarctic Peninsula over the past half-century. *Science* 308 (5721), 541–544. <https://doi.org/10.1126/science.1104235>.
- Dee, D.P., Uppala, S.M., Simmons, A.J., Berrisford, P., Poli, P., Kobayashi, S., Andrae, U., Balmaseda, M.A., Balsamo, G., Bauer, P., Bechtold, P., Beljaars, A.C.M., van de Berg, L., Bidlot, J., Bormann, N., Delsol, C., Dragani, R., Fuentes, M., Geer, A.J., Haimberger, L., Healy, S.B., Hersbach, H., Hölml, E.V., Isaksen, I., Kållberg, P., Köhler, M., Matricardi, M., McNally, A.P., Monge-Sanz, B.M., Morcrette, J.-J., Park, B.-K., Peubey, C., de Rosnay, P., Tavolato, C., Thépaut, J.-N., Vitart, F., 2011. The ERA-Interim reanalysis: configuration and performance of the data assimilation system. *Q. J. R. Meteorol. Soc.* 137 (656), 553–597. <https://doi.org/10.1002/qj.828>.
- Fahnestock, M.A., Abdalati, W., Shuman, C.A., 2002. Long melt seasons on ice shelves of the Antarctic Peninsula: an analysis using satellite-based microwave emission measurements. *Ann. Glaciol.* 34, 127–133. <https://doi.org/10.3189/172756402781817798>.
- Fang, H., Wei, S., Jiang, C., Scipal, Klaus, 2012. Theoretical uncertainty analysis of global MODIS, CYCLOPES, and GLOBECARBON LAI products using a triple collocation method. *Remote Sens. Environ.* 124, 610–621. <https://doi.org/10.1016/j.rse.2012.6352251>.
- Fettweis, X., van Ypersele, J.-P., Gallée, H., Lefebvre, F., Lefebvre, W., 2007. The 1979–2005 Greenland ice sheet melt extent from passive microwave data using an improved version of the melt retrieval XPGR algorithm. *Geophys. Res. Lett.* 34, L05502. <https://doi.org/10.1029/2006GL028787>.
- Fors, A.S., Divine, D.V., Douglis, A.P., Renner, A.H.H., Gerland, S., 2017. Signature of Arctic first-year ice melt pond fraction in X-band SAR imagery. *Cryosphere* 11, 755–771. <https://doi.org/10.5194/tc-2016-125>.
- Fraser, A.D., Young, N.W., Adams, N., 2014. Comparison of microwave backscatter anisotropy parameterizations of the Antarctic Ice Sheet using ASCAT. *IEEE Trans. Geosci. Remote Sens.* 52 (3), 1583–1595. <https://doi.org/10.1109/TGRS.2013.2252621>.
- Fraser, A.D., Nigro, M.A., Ligtenberg, S.R.M., Legresy, B., Inoue, M., Cassano, J.J., Kuipers Munneke, P., Lenaerts, J.T.M., Young, N.W., Treverrow, A., Van Den Broeke, M., Enomoto, H., 2016. Drivers of ASCAT C band backscatter variability in the dry snow zone of Antarctica. *J. Glaciol.* 62 (231), 170–184. <https://doi.org/10.1017/jog.2016.29>.
- Gruber, A., Dorigo, W.A., Crow, W., Wagner, W., 2017. Triple collocation-based merging of satellite soil moisture retrievals. *IEEE Trans. Geosci. Remote Sens.* 55 (12), 6780–6792. <https://doi.org/10.1109/TGRS.2017.2734070>.
- Hall, D.K., Nghiem, S.V., Schaaf, C.B., DiGirolamo, N.E., Neumann, G., 2009. Evaluation of surface and near-surface melt characteristics on the Greenland ice sheet using MODIS and QuikSCAT data. *J. Geophys. Res. Earth Surf.* 114, F04006. <https://doi.org/10.1029/2009JF001287>.
- Hallikainen, M.T., Ulaby, F., Abdelrazik, M., 1986. Dielectric properties of snow in the 3 to 37 GHz range. *IEEE Trans. Antennas Propag.* 34 (11), 1329–1340.
- Hogg, A.E., Gudmundsson, G.H., 2017. Impacts of the Larsen-C Ice Shelf calving event. *Nat. Clim. Chang.* 7 (8), 540–542. <https://doi.org/10.1038/nclimate3359>.
- Jacobs, S.S., Comiso, J.C., 1997. Climate variability in the Amundsen and Bellingshausen seas. *J. Clim.* 10 (4), 697–709. [https://doi.org/10.1175/1520-0442\(1997\)010<0697:CVITAA>2.0.CO;2](https://doi.org/10.1175/1520-0442(1997)010<0697:CVITAA>2.0.CO;2).
- King, J.C., Kirchgaessner, A., Bevan, S., Elvidge, A.D., Kuipers Munneke, P., Luckman, A., Orr, A., Renfrew, I.A., van den Broeke, M.R., 2017. The impact of föhn winds on surface energy balance during the 2010–2011 melt season over Larsen C Ice Shelf, Antarctica. *J. Geophys. Res. Atmos.* 122 (22), 12,062–12,076. <https://doi.org/10.1002/2017JD026809>.
- Koh, G., Jordan, R., 1995. Sub-surface melting in a seasonal snow cover. *J. Glaciol.* 41 (139), 474–482. <https://doi.org/10.3189/S002214300003481X>.
- Kuipers Munneke, P., Picard, G., van den Broeke, M.R., Lenaerts, J.T.M., van Meijgaard, E., 2012. Insignificant change in Antarctic snowmelt volume since 1979. *Geophys. Res. Lett.* 39, L01501. <https://doi.org/10.1029/2011gl050207>.
- Kuipers Munneke, P., Luckman, A.J., Bevan, S.L., Smeets, C.J.P.P., Gilbert, E., van den Broeke, M.R., Wang, W., Zender, C., Hubbard, B., Ashmore, D., Orr, A., King, J.C., Kullessa, B., 2018. Intense winter surface melt on an Antarctic Ice Shelf. *Geophys. Res. Lett.* 45 (15), 7615–7623. <https://doi.org/10.1029/2018GL077899>.
- Lenaerts, J.T.M., Lhermitte, S., Drews, R., Ligtenberg, S.R.M., Berger, S., Helm, V., Smeets, C.J.P.P., van den Broeke, M.R., van de Berg, W.J., van Meijgaard, E., Eijkelboom, M., Eisen, O., Pattyn, F., 2016. Meltwater produced by wind-albedo interaction stored in an East Antarctic ice shelf. *Nat. Clim. Chang.* 7 (1), 58–62. <https://doi.org/10.1038/nclimate3180>.
- Liang, L., Guo, H., Li, X., Cheng, X., 2013. Automated ice-sheet snowmelt detection using microwave radiometer measurements. *Polar Res.* 32 (1), 1–13. <https://doi.org/10.3402/polar.v32i0.19746>.
- Liu, H., Wang, L., Jezek, K.C., 2005. Wavelet-transform based edge detection approach to derivation of snowmelt onset, end and duration from satellite passive microwave measurements. *Int. J. Remote Sens.* 26 (21), 4639–4660. <https://doi.org/10.1080/01431160500213342>.
- Liu, H., Wang, L., Jezek, K.C., 2006. Automated delineation of dry and melt snow zones in Antarctica using active and passive microwave observations from space. *IEEE Trans. Geosci. Remote Sens.* 44 (8), 2152–2163.
- Long, D.G., Hardin, P.J., Whiting, P.T., 1993. Resolution enhancement of spaceborne scatterometer data. *IEEE Trans. Geosci. Remote Sens.* 31 (3), 700–715. <https://doi.org/10.1109/36.225536>.
- Luckman, A., Elvidge, A., Jansen, D., Kullessa, B., Kuipers Munneke, P., King, J., Barrand, N.E., 2014. Surface melt and ponding on Larsen C Ice Shelf and the impact of föhn winds. *Antarct. Sci.* 26 (6), 625–635. <https://doi.org/10.1017/S09545794102014000339>.
- Lyu, H., Mccoll, K.A., Li, X., Derksen, C., Berg, A., Black, T.A., Euskirchen, E., Loran, M., Pulliainen, J., Rautiainen, K., Rowlandson, T., Roy, A., Royer, A., Langlois, A., Stephens, J., Lu, H., Entekhabi, D., 2017. Validation of the SMAP freeze/thaw product using categorical triple collocation. *Remote Sens. Environ.* 205, 329–337. <https://doi.org/10.1016/j.rse.2017.12.007>.
- Massom, R.A., Scambos, T.A., Bennetts, L.G., Reid, P., Squire, V.A., Stammerjohn, S.E., 2018. Antarctic ice shelf disintegration triggered by sea ice loss and ocean swell. *Nature* 558 (7710), 383–389. <https://doi.org/10.1038/s41586-018-0212-1>.
- McColl, K.A., Roy, A., Derksen, C., Konings, A.G., Alemohammed, S.H., Entekhabi, D., 2016. Triple collocation for binary and categorical variables: application to validating landscape freeze/thaw retrievals. *Remote Sens. Environ.* 176, 31–42. <https://doi.org/10.1016/j.rse.2016.01.010>.
- Mortin, J., Howell, S.E.L., Wang, L., Derksen, C., Svensson, G., Graversen, R.G., Schröder, T.M., 2014. Extending the QuikSCAT record of seasonal melt-freeze transitions over Arctic sea ice using ASCAT. *Remote Sens. Environ.* 141, 214–230. <https://doi.org/10.1016/j.rse.2013.11.004>.
- O'Carroll, A.G., Eyre, J.R., Saunders, R.W., 2008. Three-way error analysis between AATSR, AMSR-E, and in situ sea surface temperature observations. *J. Atmos. Ocean. Technol.* 25 (7), 1197–1207. <https://doi.org/10.1175/2007JTECH0542.1>.
- Oliva, M., Navarro, F., Hrbáček, F., Hernández, A., Nývlt, D., Pereira, P., Ruiz-Fernández, J., Trigo, R., 2017. Recent regional climate cooling on the Antarctic Peninsula and associated impacts on the cryosphere. *Sci. Total Environ.* 580, 210–223. <https://doi.org/10.1016/j.scitotenv.2016.12.030>.
- Parajka, J., Scipal, K., Merz, R., Blöschl, G., Wagner, W., Kidd, R., Bartalis, Z., Naeimi, V., 2005. Spatial and temporal dynamics of soil moisture in ungauged basins. In: *Interim Report. Hydrology of Austria Programme (HÖ), Austrian Academy of Sciences*.
- Parisi, F., Strino, F., Nadler, B., Kluger, Y., 2014. Ranking and combining multiple predictors without labeled data. *Proc. Natl. Acad. Sci. U. S. A.* 111 (4), 1253–1258. <https://doi.org/10.1073/pnas.1219097111>.
- Picard, G., Fily, M., 2006. Surface melting observations in Antarctica by microwave radiometers: correcting 26-year time series from changes in acquisition hours. *Remote Sens. Environ.* 104 (3), 325–336.
- Rau, F., Mauz, F., De Angelis, H., Jaña, R., Neto, J.A., Skvarca, P., Vogt, S., Saurer, H., Gossmann, H., 2004. Variations of glacier frontal positions on the northern Antarctic Peninsula. *Ann. Glaciol.* 39, 525–530. <https://doi.org/10.3189/172756404781814212>.
- Ridley, J., 1993. Surface melting on Antarctic Peninsula ice shelves detected by passive microwave sensors. *Geophys. Res. Lett.* 20 (23), 2639–2642. <https://doi.org/10.1029/93GL02611>.
- Rignot, E., Jacobs, S., Mouginot, J., Scheuchl, B., 2013. Ice-shelf melting around Antarctica. *Science* 341 (6143), 266–270. <https://doi.org/10.1126/science.1235798>.
- Roebeling, R.A., Wolters, E.L.A., Meirink, J.F., Leijnse, H., 2012. Triple collocation of

- summer precipitation retrievals from SEVIRI over Europe with gridded rain gauge and weather radar data. *J. Hydrometeorol.* 13 (5), 1552–1566. <https://doi.org/10.1175/jhm-d-11-089.1>.
- Scambos, T., Hulbe, C., Fahnestock, M., Bohlander, J., 2000. The link between climate warming and break-up of ice shelves in the Antarctic Peninsula. *J. Glaciol.* 46 (154), 516–530. <https://doi.org/10.3189/172756500781833043>.
- Scambos, T.A., Haran, T.M., Fahnestock, M.A., Painter, T.H., Bohlander, J., 2007. MODIS-based Mosaic of Antarctica (MOA) data sets: continent-wide surface morphology and snow grain size. *Remote Sens. Environ.* 111, 242–257. <https://doi.org/10.1016/j.rse.2006.12.020>.
- Scott, R.C., Lubin, D., Vogelmann, A.M., Kato, S., 2017. West antarctic ice sheet cloud cover and surface radiation budget from NASA A-Train satellites. *J. Clim.* 30 (16), 6151–6170. <https://doi.org/10.1175/JCLI-D-16-0644.1>.
- Scott, R.C., Nicolas, J.P., Bromwich, D.H., Norris, J.R., Lubin, D., 2018. Meteorological drivers and large-scale climate forcing of West Antarctic surface melt. *J. Clim.* 32 (3), 665–684. <https://doi.org/10.1175/JCLI-D-18-0233.1>.
- Smith, L.C., 2003. Melting of small Arctic ice caps observed from ERS scatterometer time series. *Geophys. Res. Lett.* 30 (20), 2034. <https://doi.org/10.1029/2003GL017641>.
- Steffen, K., Abdalati, W., Stroeve, J., 1993. Climate sensitivity studies of the Greenland ice sheet using satellite AVHRR, SMMR, SSM/I and in situ data. *Meteorol. Atmos. Phys.* 51 (3–4), 239–258. <https://doi.org/10.1007/BF01030497>.
- Steig, E.J., 2016. Cooling in the Antarctic. *Nature* 535 (7612), 358–359. <https://doi.org/10.1038/535358a>.
- Steiner, N., Tedesco, M., 2014. A wavelet melt detection algorithm applied to enhanced-resolution scatterometer data over Antarctica (2000–2009). *Cryosphere* 8, 25–40. <https://doi.org/10.5194/tc-8-25-2014>.
- Stiles, W.H., Ulaby, F.T., 1980. The active and passive microwave response to snow parameters: 1. Wetness. *J. Geophys. Res.* 85 (C2), 1037–1044. <https://doi.org/10.1029/JC085iC02p01037>.
- Stoffelen, A., 1998. Toward the true near-surface wind speed: error modeling and calibration using triple collocation. *J. Geophys. Res.* 103 (C4), 7755–7766. <https://doi.org/10.1029/97JC03180>.
- Stroeve, J.C., Mioduszewski, J.R., Rennermalm, A., Boisvert, L.N., Tedesco, M., Robinson, D., 2017. Investigating the local scale influence of sea ice on Greenland surface melt. *Cryosphere* 11, 2363–2381. <https://doi.org/10.5194/tc-2017-65>.
- Su, C.H., Ryu, D., Crow, W.T., Western, A.W., 2014. Beyond triple collocation: applications to soil moisture monitoring. *J. Geophys. Res. Atmos.* 119 (11), 6419–6439. <https://doi.org/10.1002/2013JD021043>.
- Tedesco, M., 2007. Snowmelt detection over the Greenland ice sheet from SSM/I brightness temperature daily variations. *Geophys. Res. Lett.* 34, L02504. <https://doi.org/10.1029/2006GL028466>.
- Tedesco, M., 2009. Assessment and development of snowmelt retrieval algorithms over Antarctica from K-band spaceborne brightness temperature (1979–2008). *Remote Sens. Environ.* 113 (5), 979–997. <https://doi.org/10.1016/j.rse.2009.01.009>.
- Tedesco, M., Monaghan, A.J., 2009. An updated Antarctic melt record through 2009 and its linkages to high-latitude and tropical climate variability. *Geophys. Res. Lett.* 36, L18502. <https://doi.org/10.1029/2009GL039186>.
- Trusel, L.D., Frey, K.E., Das, S.B., 2012. Antarctic surface melting dynamics: enhanced perspectives from radar scatterometer data. *J. Geophys. Res. Atmos.* 117, F02023. <https://doi.org/10.1029/2011JF002126>.
- Trusel, L.D., Frey, K.E., Das, S.B., Peter Kuipers, M., van den Broeke, M., 2013. Satellite-based estimates of Antarctic surface meltwater fluxes. *Geophys. Res. Lett.* 40 (23), 6148–6153. <https://doi.org/10.1002/2013GL058138>.
- Trusel, L.D., Frey, K.E., Das, S.B., Karnauskas, K.B., Kuipers Munneke, P., van Meijgaard, E., van den Broeke, M.R., 2015. Divergent trajectories of Antarctic surface melt under two twenty-first-century climate scenarios. *Nat. Geosci.* 8 (12), 927–932. <https://doi.org/10.1038/ngeo2563>.
- Tsai, W.Y., Nghiem, S.V., Huddleston, J.N., Spencer, M.W., Stiles, B.W., West, R.D., 2000. Polarimetric scatterometry: a promising technique for improving ocean surface wind measurements from space. *IEEE Trans. Geosci. Remote Sens.* 38 (4), 1903–1921. <https://doi.org/10.1109/36.851773>.
- Turner, J., Colwell, S.R., Marshall, G.J., Lachlan-Cope, T.A., Carleton, A.M., Jones, P.D., Lagun, V., Reid, P.A., Iagovkina, S., 2004. The SCAR READER project: toward a high-quality database of mean Antarctic meteorological observations. *J. Clim.* 17 (14), 2890–2898. [https://doi.org/10.1175/1520-0442\(2004\)017<2890:TSRPTA>2.0.CO;2](https://doi.org/10.1175/1520-0442(2004)017<2890:TSRPTA>2.0.CO;2).
- Turner, J., Maksym, T., Phillips, T., Marshall, G.J., Meredith, M.P., 2013. The impact of changes in sea ice advance on the large winter warming on the western Antarctic Peninsula. *Int. J. Climatol.* 33, 852–861. <https://doi.org/10.1002/joc.3474>.
- Turner, J., Barrand, N.E., Bracegirdle, T.J., Convey, P., Hodgson, D.A., Jarvis, M., Jenkins, A., Marshall, G., Meredith, M.P., Roscoe, H., Shanklin, J., French, J., Goosse, H., Guglielmin, M., Gutt, J., Jacobs, S., Kennicutt, M.C., Masson-Delmotte, V., Mayewski, P., Navarro, F., Robinson, S., Scambos, T., Sparrow, M., Summerhayes, C., Speer, K., Klepikov, A., 2014. Antarctic climate change and the environment: an update. *Polar Rec.* 50 (3), 237–259. <https://doi.org/10.1017/S0032247413000296>.
- Turner, J., Lu, H., White, I., King, J.C., Phillips, T., Hosking, J.S., Bracegirdle, T.J., Marshall, G.J., Mulvaney, R., Deb, P., 2016. Absence of 21st century warming on Antarctic Peninsula consistent with natural variability. *Nature* 535 (7612), 411–415. <https://doi.org/10.1038/nature18645>.
- van den Broeke, M., 2005. Strong surface melting preceded collapse of Antarctic Peninsula ice shelf. *Geophys. Res. Lett.* 32, L12815. <https://doi.org/10.1029/2005GL023247>.
- van den Broeke, M., van de Berg, W., van Meijgaard, E., Reijmer, C., 2006. Identification of Antarctic ablation areas using a regional atmospheric climate model. *J. Geophys. Res.* 111, D18110. <https://doi.org/10.1029/2006JD007127>.
- van den Broeke, M., König-Langlo, G., Picard, G., Kuipers Munneke, P., Lenaerts, J., 2010. Surface energy balance, melt and sublimation at Neumayer Station, East Antarctica. *Antarct. Sci.* 22 (1), 87–96. <https://doi.org/10.1017/S0954102009990538>.
- Vaughan, D.G., 2006. Recent trends in melting conditions on the Antarctic Peninsula and their implications for ice-sheet mass balance and sea level. *Arct. Antarct. Alp. Res.* 38 (1), 147–152. [https://doi.org/10.1657/1523-0430\(2006\)038\[0147:RTIMCO\]2.0.CO;2](https://doi.org/10.1657/1523-0430(2006)038[0147:RTIMCO]2.0.CO;2).
- Vaughan, D.G., Marshall, G.J., Connolley, W.M., Parkinson, C., Mulvaney, R., Hodgson, D.A., King, J.C., Pudsey, C.J., Turner, J., 2003. Recent rapid regional climate warming on the Antarctic Peninsula. *Clim. Chang.* 60 (3), 243–274. <https://doi.org/10.1023/A:1026021217991>.
- Wang, X., Li, X., Wang, C., Li, X., 2018. Antarctic ice-sheet near-surface snowmelt detection based on the synergy of SSM/I data and QuikSCAT data. *Geosci. Front.* 9 (3), 955–963. <https://doi.org/10.1016/J.GSF.2017.09.007>.
- Weatherhead, E.C., Reinsel, G.C., Tiao, G.C., Meng, X.-L., Choi, D., Cheang, W.-K., Keller, T., Deluisi, J., Wuebbles, D.J., Kerr, J.B., Miller, A.J., Oltmans, S.J., Frederick, J.E., 1998. Factors affecting the detection of trends: statistical considerations and applications to environmental data. *J. Geophys. Res.* <https://doi.org/10.1029/98JD00995>.
- Xu, J., Shu, H., 2015. The triple-collocation-based fusion of in-situ and satellite remote sensing data for snow depth retrieval. *Geomatics Inf. Sci. Wuhan Univ.* 40 (4), 469–473.
- Zheng, L., Zhou, C., Liu, R., Sun, Q., 2018. Antarctic snowmelt detected by diurnal variations of AMSR-E brightness temperature. *Remote Sens.* 10 (9), 1391. <https://doi.org/10.3390/rs10091391>.
- Zhou, C., Zheng, L., 2017. Mapping radar glacier zones and dry snow line in the Antarctic Peninsula using Sentinel-1 images. *Remote Sens.* 9 (11), 1171. <https://doi.org/10.3390/rs9111171>.
- Zhou, C., Zheng, L., Sun, Q., Liu, R., 2019. Amery Ice Shelf surface snowmelt detected by ASCAT and Sentinel-1. *Remote Sens. Lett.* 10 (5), 430–438. <https://doi.org/10.1080/2150704X.2018.1553317>.
- Zwally, H.J., Fiegles, S., 1994. Extent and duration of Antarctic surface melting. *J. Glaciol.* 40 (136), 463–475. <https://doi.org/10.1017/S0022143000012338>.